The Net Discharge Mechanism of the VB_2/Air Battery

Jessica Stuart,[a,*] Amelia Hohenadel,[a] Xuguang Li,[b] Han Xiao,[b] Jeff Parkey,[b] Christopher P. Rhodes,[c,z] and Stuart Licht[a,,z]**

[a]*Department of Chemistry, George Washington University, Washington, D.C. 20052, USA*
[b]*Lynntech, College Station, Texas 77845, USA*
[c]*Department of Chemistry and Biochemistry, Texas State University, San Marcos, Texas 78666, USA*

The electrochemical discharge of VB_2 is a unique process that involves the multiple electron per molecule oxidation of the tetravalent transition metal ion, V ($+4 \rightarrow +5$), and each of the two borons $2\times$B ($-2 \rightarrow +3$), corresponding to a net 11 electron discharge mechanism of the VB_2/air cell as described by the overall cell reaction: $VB_2 + 11/4O_2 \rightarrow B_2O_3 + \frac{1}{2}\ V_2O_5$. However, in the presence of alkaline electrolytes, the discharge products include alkali salts associated with vanadaic and boric acid. In this study, we used FTIR, XRD, and coulombic efficiency measurements to probe the discharge products of high capacity cells and isolate KVO_3 as the principal vanadium discharge product. Additionally, we show that $K_2B_4O_7$ is the probable borate product. From FTIR analysis in KOH electrolyte, it is evident that the alkaline VB_2/air discharge reaction is: $VB_2 + 11/4O_2 + 2KOH \rightarrow \frac{1}{2}\ K_2B_4O_7 + KVO_3 + H_2O$. XPS shows that the surface structure of nanoscopic VB_2 is very different from macroscopic VB_2, which may contribute to the improved electrochemical properties of the nanoscopic material. The understanding of the discharge process and factors affecting performance contribute to furthering the development of extremely high capacity VB_2/air batteries that utilize multi-electron processes.

Manuscript submitted October 6, 2014; revised manuscript received November 11, 2014. Published November 26, 2014.

Metallic zinc has been used as an anode material in the majority of aqueous primary systems due to zinc metal's high two-electron oxidation capacity and effective discharge. The zinc-carbon battery, known as the Leclanché cell, was first introduced in the 19th century as a low-cost solution for early energy storage needs. The zinc cell, which produced approximately 65 Wh kg^{-1}, was ideal only for low-rate discharges.[1,2] Until the development of the zinc/alkaline/manganese dioxide battery and the zinc/air cell, there was little improvement in primary batteries. The alkaline Zn/MnO_2 cell has since dominated primary electrochemical storage, providing 145 Wh kg^{-1}. Although more expensive than the zinc-carbon battery, the alkaline cell improved performance by increasing energy densities and power capabilities. The zinc/air battery, using external O_2 as the battery active cathode reactant further improves the energy density of primary battery systems. It would be useful for electronic devices to have even higher energy storage densities than that available with zinc/air batteries.[3] Most metal/air batteries to date have been unsuccessful in reaching the high-energy densities that are made possible by multi-electron oxidations, due to material passivation or chemical instabilities.[4]

To provide high energy density cells, there has been an effort to develop high-capacity multi-electron per molecule charge storage processes.[5–21] Vanadium diboride (VB_2) undergoes a multiple electron oxidation process, which to its completion involves an extraordinary 11 electron per molecule oxidation, including oxidation of the tetravalent transition metal ion, V($+4 \rightarrow +5$), and each of the two borons 2xB($-2 \rightarrow +3$). VB_2 has an intrinsic gravimetric capacity of 4060 Ah kg^{-1}, which is five-fold higher than that of the Zn anode electrode (820 Ah kg^{-1}). The intrinsic volumetric anodic capacity of the VB_2 anode (20.7 kAh L^{-1}) is tenfold higher than that of the lithium anode (2.06 kAh L^{-1}).[13–21]

A VB_2 anode within a battery can be coupled with oxygen from external air to provide extremely high energy density VB_2/air batteries.[17] The anode half cell, cathode half cell, and full cell reactions based on generalized discharge products[19] are as follows:

$$\text{Anode}: VB_2 + 11OH^- \rightarrow 1/2V_2O_5 + B_2O_3 + 11/2\ H_2O + 11e^- \quad [1]$$

$$\text{Cathode}: 11/4O_2 + 11/2\ H_2O + 11e^- \rightarrow 11OH^- \quad [2]$$

$$\text{Cell}: VB_2 + 11/4O_2 \rightarrow B_2O_3 + 1/2\ V_2O_5 \quad E_{cell} = 1.55\ V \quad [3]$$

The VB_2/air battery has a theoretical discharge potential of 1.55 V, as calculated from the thermodynamic free energy of the cell reactants and products.[19] The VB_2/air battery's intrinsic volumetric energy density of 32 kWh L^{-1} is substantially greater than that of gasoline (<10 kWh L^{-1}) and has an intrinsic specific energy of 5,300 kWh kg^{-1}, which is four times higher than the theoretical specific energy of zinc/air batteries (1,353 kWh kg^{-1}). The VB_2/air couple uses an alkaline electrolyte, such as aqueous KOH or NaOH. Oxygen from the air reacts at the cathode in a manner similar to that of the zinc/air cell.[3] Concentrated aqueous hydroxide electrolytes ranging from 8 molar to saturated KOH or NaOH yield a similar electrochemical discharge in the VB_2/air cell.[18,19] The VB_2/air cell shows an experimental open circuit potential of ~1.3 V, and under load, the cell can release its capacity over a flat, highly singular discharge potential plateau.

Self-discharge is of paramount important for the practical operation of a battery, and similar to Zn anodes, the VB_2 anode can react with the electrolyte under open circuit potential. In Zn/air batteries, the self-discharge loss was until recently mitigated by the addition of several percent mercuric oxide. More recently, the mercury additives have been replaced with compounds such as polyacrylic acid (i.e. Carbopol), and other Zn/air self-discharge mitigation strategies include alloying, coating with Al_2O_3 and various organic corrosion inhibitors.[22] Our prior efforts to stabilize VB_2 have involved using a zirconia overlayer to prevent corrosion of the boride surface while also allowing charge transfer during the anodic discharge process. Using this approach for macroscopic VB_2, we have been able to largely mitigate the VB_2 self-discharge through using a zirconia overlayer.[12,17] Stored at 45°C for one week, an uncoated VB_2 alkaline anode loses 10% of its original charge capacity, however with a 1% ZrO_2 coating the anode retains 100% of that capacity.[17]

Synthesis of nanoscopic VB_2 has been explored,[18,19,23] and can improve anode performance in VB_2/air batteries.[18,19,21] Its preparation from elemental vanadium and boron powders in a planetary ball mill is straightforward, and this nano-VB_2 is anodically active in electrochemical media.[19] As reported, the planetary ball mill synthesis reaction of elemental vanadium and boron yields VB_2 as characterized by XRD (X-ray diffraction).[19] Recently, we reported on the improved voltage and 11 electron discharge efficiency of 5 mAh VB_2/air batteries using this nanoscopic compared to macroscopic particle sized VB_2 within the anode construction.[19–21] As seen in Figure 1, nanoscopic VB_2 cells discharged to 70–74% coulombic efficiency over a load 3000 Ω and exhibited an initial potential of 0.9 V. This compares to

*Electrochemical Society Student Member.
**Electrochemical Society Active Member.
zE-mail: cprhodes@txstate.edu; slicht@gwu.edu

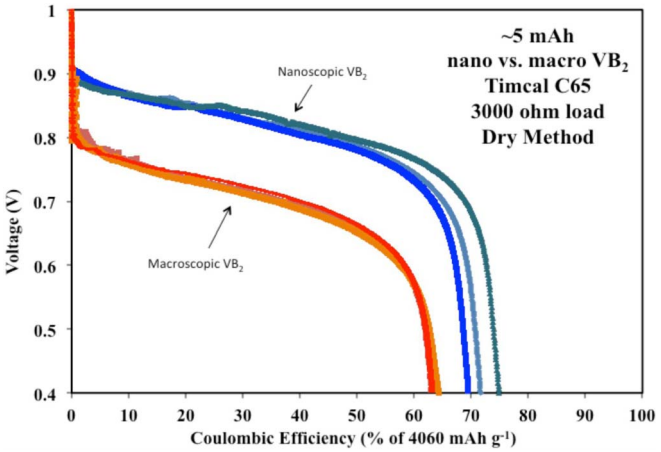

Figure 1. Comparison of VB_2/air cells containing either macroscopic or nanoscopic VB_2 with a capacity of 5 mAh discharged at a constant load of 3000 Ω.[21]

only 63% coulombic efficiency and an initial potential of 0.8 V for the macroscopic VB_2 cells. The Equation 1 oxidation products are generalized as B_2O_3 and V_2O_5, which are the respective anhydride salts of boric acid (H_3BO_3, pK1,2,3 = 9.1, 12.7 and 13.8) and vanadaic acid (H_3VO_4, pK1,2,3 = 3.8, 7.8 and 13.0). In solution, the products will vary with hydroxide concentration and depth of discharge, including hydrogen and metal cation containing species, such as in either a KOH or NaOH electrolyte: $K_xH_zBO_3^{3-x-z}$ or $Na_xH_zBO_3^{3-x-z}$ (where x ranges from 0 to 3, and z from 0 to 3 - x), as well as polymeric species, such as related to the boric condensation reaction forming borax species: $Na_yB_4O_7^{2-y}$, $K_yB_4O_7^{2-y}$, and analogous vanadium species. In this study, we isolated the vanadium active discharge product from a potassium hydroxide electrolyte as well as the boron discharge product formed in a potassium hydroxide electrolyte of the VB_2/air cell to advance understanding of this high-energy capacity battery.

We had initially been unsuccessful in scaling the battery to thicker anodes to allow for higher intrinsic capacity. This limited the quantity of extractable discharge product for analysis. In this study, this limitation is overcome yielding larger quantities of the VB_2/air battery discharge product. This provides a path to analyzing speciation of the product and a net alkaline discharge mechanism of the battery. In this paper, we also introduce XPS measurements that compare the macroscopic to nanoscopic vanadium diboride and provide strong evidence for a VB_2 surface-based understanding of the higher observed discharge voltage of the nanoscopic VB_2/air batteries.

Experimental

Nanoscopic VB_2 synthesis.— Nanoscopic VB_2 was synthesized mechanochemically using vanadium powder (Alfa Aesar) and boron powder (Alfa Aesar) based on methods previously published by Licht et al. [8]. In a controlled argon atmosphere glove box system (Vacuum Atmospheres, Nexus-II), 0.500 g of vanadium and 0.212 g of boron power were measured and transferred into a tungsten carbide milling chamber along with ten tungsten carbide balls, ten millimeters in diameter. The milling vessel was sealed, removed from the glove box, and placed into a Retsch PM 100 planetary ball mill set to 600 rpm and allowed to run for four hours. After the vanadium diboride cooled to room temperature, the material was then collected in the glove box and the mass was measured.

The electrochemical performance of the VB_2 anode, as well as the composite anode, was investigated. Coulombic efficiency is the percentage of the measured capacity compared to the theoretical (intrinsic) anode discharge capacity of the VB_2 anode.

Anode fabrication.— Anodes were prepared using nanoscopic VB_2, synthesized in-laboratory as described above, or commercially available, macroscopic VB_2 (American Elements Organo-Metallics), carbon black (TIMCAL C-NERGY SUPER C65), and KOH pellets (Alfa Aesar). Panasonic PR675H batteries were used as a test bed for electrode fabrication to perform electrochemical tests. The cell fabricated is as previously delineated.[21] In brief, the air electrode from the Panasonic battery is kept intact and reused. The Zn anode of the Panasonic cells was removed by opening the existing cell, removing the anode active material, and using the separator and cathode as received for the VB_2/air battery. VB_2 electrodes were prepared first by mixing 70 wt% active material (VB_2) and 30 wt% carbon black, then measuring the appropriate amount of dry material, and lastly spreading the mixture with isopropyl alcohol and allowing the working electrode to dry. An 8M KOH electrolyte solution was used. The cell was then closed with the cap in reverse so that the anodic material was in contact with the electrolyte.

Once the fabrication process had been completed, cells were discharged at constant loads as indicated in the results and discussion. The change in voltage with time during discharge was measured using NI LabVIEW 2010 and NI USB-6210 multifunction data acquisition.

XRD analysis.— X-ray diffraction (XRD) measurements were performed with a Rigaku MiniFlex. Samples were prepared by loading the crushed powders on a round zero background holder containing a depression in the middle and spread by either isopropyl alcohol or petroleum jelly. Spectra were obtained using the Rigaku powder diffraction analysis package, PDXL. Further analysis was completed with comparison of the obtained spectra to the Inorganic Crystal Structure Database (ICSD) online.

XPS analysis.— X-ray photoelectron spectroscopy (XPS) measurements were obtained at the University of South Carolina on a Kratos AXIS Ultra DLD XPS system equipped with a hemispherical energy analyzer and a monochromatic Al K source, which was operated at 15 keV and 150 W. XPS fitting was carried out by using XPSPEAK Version 4.1 software. Anodic material of the macroscopic and nanoscopic VB_2 was tested prior to and after discharging at a load of 3,000 ohm. The anodic composite consisted of a mixture of 70% VB_2, equivalent to a capacity of 5 mAh, and 30% C65 carbon. Cells used for XPS analysis were discharged using an Arbin Instruments battery tester controlled by MITS software.

Solubility measurements.— 5 mL of 8 molar KOH were transferred to two 10 mL beakers and placed on a stir plate under constant stirring. Potassium metavanadate, KVO_3, or boron oxide, B_2O_3, were weighed and periodically transferred to either beaker, and dissolved until the two solutions became saturated. Both beakers were covered and left to stir for 48 hours. Vacuum filtration was used to collect KVO_3 (Alfa Aesar 99.9%) and B_2O_3 (Alfa Aesar 99%) that remained undissolved. Filter papers with the solid excess were left overnight to dry in a hood then weighed. The solubility was determined by subtracting the undissolved KVO_3 and B_2O_3 from the total mass added to each solution then dividing by volume of KOH. FTIR were measured for the salts and for $K_2B_4O_7{\cdot}4H_2O$ (Alfa Aesar 99%), KVO_3 (Alfa Aesar 99.9%) and K_3VO_4 (Alfa Aesar 99.9%).

FTIR analysis.— Characterization of spent battery material and battery discharge products was completed via Fourier-Transform Infrared Spectroscopy (FT-IR). Weighed samples to be analyzed were ground thoroughly with KBr by mortar and pestle. By means of a hydraulic press, 150 mg of the sample mixture was pressed under 7 tons of pressure for 5 minutes using a Perkin-Elmer 13 mm die set to form a KBr pellet containing the sample for analysis. Composition of the KBr pellets varied between 0.1 weight percent and 1 weight percent of the sample depending on the opaqueness of the sample. Filtrates for B_2O_3 in KOH and H_2O were measured using attenuated total reflectance infrared spectroscopy (ATR-FTIR), as an alternative method to transmission spectroscopy. FTIR spectra were measured by Perkin-Elmer Spectrum 100 with a resolution of 4 cm^{-1} and between 16 and 32 scans per spectrum. A baseline correction was performed with the automatic baseline correction tool offered with the Perkin-Elmer Spectrum software package.

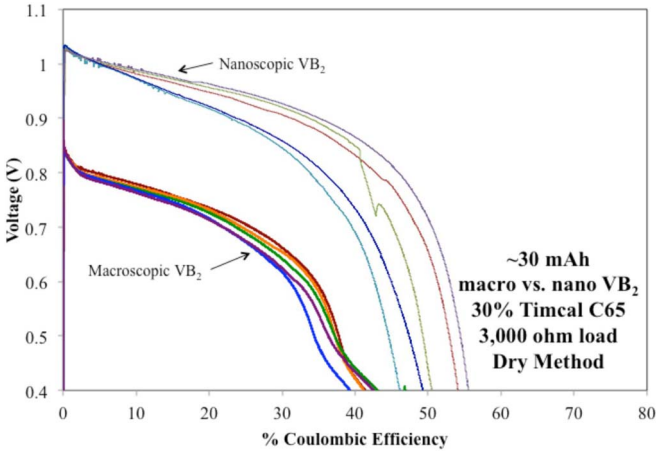

Figure 2. Comparison of higher capacity ~30 mAh anode, compared to the 5 mAh in Figure 1. Macroscopic (bottom curves) or nanoscopic (top curves) 1 cm diameter VB_2/air batteries discharged over a 3000 Ω load. Discontinuity in the green colored discharge curve is symptomatic of an infrequent, but observed poor electrical contact to data acquisition rather than an intrinsic property of the cell.

Results and Discussion

Utilizing high capacity VB_2 anode/air batteries.— The unusually high gravimetric anodic capacity coupled with the characteristic high density of VB_2, 5.10 g cm^{-3}, results in a large volumetric capacity of 20,700 mAh cm^{-3}. Hence, only small quantities of VB_2 are required for extended battery discharge. A five mAh (1 cm diameter) button cell contains only ~1 mg of VB_2, which yields little discharge product. This small amount of discharge product is a direct result of the attractive high capacity of the anode. However, the small quantities posed challenges to effective characterization of that discharge product. Initial attempts to scale-up were ineffective resulting in rapid decreases in coulombic efficiency as the anode thickness was increased several fold.

Recent improvements to the cell fabrication process including upgrades to the gas regeneration in the glove box to better exclude oxygen and better control of the ball mill process have significantly improved scaled-up cell performance. Here, we show that a 6-fold increase in the packed capacity of the 1 cm diameter cell results in a reproducible cell with a relatively small decrease in coulombic efficiency, and further enhancement in the initial cell discharge potential for that of the nanoscopic VB_2 anode (greater than 1.0 V) as shown in Figure 2. The coulombic efficiency of the nanoscopic material has fallen from ~70 to ~52% with scale-up; however, the 600% increase in packed anode post-discharge provides sufficient discharge product for analysis. Using the 30 mAh cells that contained thicker anodes, the nanoscopic material still showed significantly higher voltages and capacities compared with the macroscopic material.

XPS of the macroscopic and nanoscopic VB_2/air battery anodic active material.— To further understand the significant difference in the electrochemical discharge of the nanoscopic and macroscopic material, XPS measurements were carried out to characterize the concentrations and oxidation states of the elements at the surface region (top ~10 nm of the surface) of the unreacted macroscopic and nanoscopic VB_2 materials (prior to discharge).

The XPS showed clear differences in the atomic concentration of V, B, and O at the surface region of the macroscopic and nanoscopic VB_2, as shown in Table I. From the data, comparable amounts of V were observed for both macroscopic and nanoscopic VB_2. However, the concentration of B at the surface of macroscopic VB_2 is much lower than that on nanoscopic VB_2. In contrast, the oxygen concentration on macroscopic VB_2 is much higher compared to nanoscopic VB_2.

The V2p, B1s, and O1s regions of the XPS spectra were evaluated to determine the specific species present at the surface region

Table I. Surface concentrations of macroscopic and nanoscopic VB_2 from XPS analysis.

Sample	Element (Region)	Atomic concentration (%)
Macro VB_2	Vanadium ($V2p^{3/2}$)	19.8
	Boron (B1s)	12.0
	Oxygen (O1s)	68.2
Nano VB_2	Vanadium ($V2p^{3/2}$)	17.3
	Boron (B1s)	46.3
	Oxygen (O1s)	36.4

of the macroscopic and nanoscopic VB_2 materials, as presented in Figure 3. The peak positions from fitting, their relative concentrations, and assignments for the V, B, and O species are shown in Table II.

The V2p, B1s, and O1s regions of the XPS spectra show significant differences in the type and relative concentration of species present at the surface of macroscopic and nanoscopic VB_2. As shown in Figure 3a, in the V2p region, the spectra are composed of a pair of $V2p^{1/2}$ and $V2p^{3/2}$ peaks due to spin-orbit peak splitting. As presented in Figure 3c, the $V2p^{3/2}$ peak of the macroscopic VB_2 can be fitted to two peaks at 516.3 eV and 517.6 eV, which are attributed to VO_2/V_2O_4 (V^{4+}) and V_2O_5 (V^{5+}) species respectively.[24] In contrast, the $V2p^{3/2}$ peak of nano-VB_2 contains three peaks from fitting analysis as shown in Figure 3b, and the peak positions of 512.5 eV, 513.6 eV, and 515.4 eV are attributed to elemental vanadium, VB_2, and a V_2O_3 (V^{3+}) species respectively.[24] The peak position of 513.6 eV attributed to VB_2 is similar to the reported value of 513.7 eV for VB_2 prepared from a high temperature synthesis process.[23] The existence of elemental V at the surface of nano-VB_2 is due to the un-reacted vanadium precursor. Interestingly, while the V-containing species at the surface of macroscopic VB_2 are vanadium oxides, nanoscopic VB_2 contains VB_2 at the surface in addition to elemental vanadium and a vanadium oxide species.

As shown in Figures 3d and 3f, the XPS spectra of macroscopic VB_2 in the B1s region can be fitted to peaks at 193.9 eV and 192.8 eV, assigned to H_3BO_3 and B_2O_3, respectively.[24] For nano-VB_2, shown in Figure 3e, the B1s spectra can be fitted to three peaks at 187.3 eV, 187.8 eV, and 192.3 eV, which are attributed to B(0), VB_2, and B_2O_3, respectively. The B1s peak position of 187.8 eV for boron in VB_2 is in the same range but slightly lower than the peak position reported for VB_2 (188.2 eV),[23] which indicates a slightly different chemical environment for boride at the surface of nano-VB_2. The existence of boron in nano-VB_2 is due to the un-reacted boron precursor.

The XPS spectra in the O1s region was also analyzed and is shown in Figures 3g–3i. Oxygen detected by XPS on the surface of VB_2 may be introduced by surface oxidation of B and V, as well as the adsorption of H_2O. As shown in Figure 3i, fitting analysis of macroscopic VB_2 shows three peaks at 530.3 eV, 531.0 eV, and 532.7 eV attributed to oxygen in VO_2(V^{4+}) oxide, V_2O_5 (V^{5+}) oxide, and B_2O_3 respectively.[24] Nano-VB_2 exhibits peaks at 530.5 eV and 532.1 eV attributed to oxygen within VO_2(V^{4+}) oxide or V_2O_3(V^{3+}) oxide, and B_2O_3 respectively.[24] It should be noted that, the O1s peak of oxygen from H_2O has a binding energy of 534.4 ± 1.8 eV, which is not observed in our case. Therefore, the oxygen present in both macroscopic and nanoscopic VB_2 is not from adsorbed water.

As shown in Figure 3 and Tables I and II, it is clear from the XPS analysis that nanoscopic VB_2 has a very different surface structure compared with macroscopic VB_2. Interestingly, the macroscopic VB_2 does not show the presence of VB_2 on the surface, but rather it shows oxides. In contrast, the nanoscopic VB_2 shows the presence of VB_2 at the surface region.

The surface structure of both macroscopic and nanoscopic VB_2 is related to the synthetic conditions, additional surface treatments, and atmospheric storage conditions (oxygen and/or water). The low observed surface oxygen content of nanoscopic VB_2 is related to the synthesis and storage conditions used: elemental vanadium and boron were combined in a glove box with ≤10 ppm H_2O and O_2, sealed and transferred to the ball mill, and then transferred back into the glove

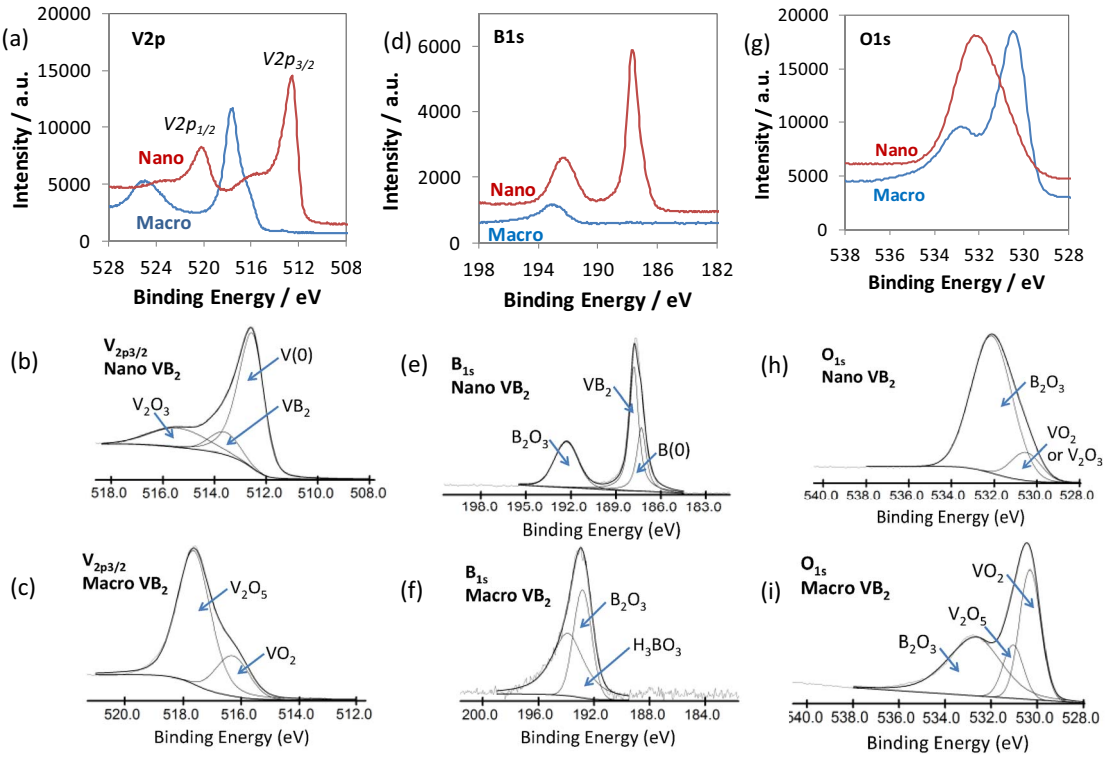

Figure 3. XPS spectra and fitted peaks for macroscopic and nanoscopic VB_2 in the V2p (a,b,c) B1s (d,e, f) and O1s (g, h, i) regions.

box. Although handled in our laboratory in the glove box similar to nanoscopic VB_2, commercial macroscopic VB_2 may have higher surface oxygen content due to synthetic or prior storage conditions.

The data and analysis shows that the as-prepared materials have very different surface structures, which in turn affects the electrochemical properties. Since the macroscopic VB_2 has a significantly higher concentration of oxides present at the surface region compared with nanoscopic VB_2, this may result in an additional resistive layer that affects the ability of hydroxides to interact with the underlying VB_2 structure. The additional resistance resulting from the oxide layer is supported by our prior work, which showed that the interfacial charge transfer resistance of the macroscopic material was higher for the macroscopic VB_2 compared to nanoscopic VB_2.[20]

Table II. Relative concentrations of surface V, B and O species for macroscopic and nanoscopic VB_2 obtained from fitting of XPS spectra.

Element	Sample	Binding Energy (eV)	Relative concentration (%)	Assigned Species[24]
V	Nano	512.5	70.7	V (elemental)
	VB_2	513.6	11.7	VB_2
		515.4	17.6	V_2O_3 (V^{3+})
	Macro	516.3	20.8	VO_2/V_2O_4 (V^{4+})
	VB_2	517.6	79.2	V_2O_5 (V^{5+})
B	Nano	187.3	23.2	B(0)
	VB_2	187.8	44.2	VB_2
		192.3	32.6	B_2O_3
	Macro	192.8	41.5	B_2O_3
	VB_2	193.9	58.5	H_3BO_3
O	Nano	530.5	13.0	VO_2 (V^{4+})or V_2O_3(V^{3+})
	VB_2	532.1	87.0	B_2O_3
	Macro	530.3	36.1	VO_2 (V^{4+})
	VB_2	531.0	14.4	V_2O_5 (V^{5+})
		532.7	49.5	B_2O_3

XRD of the VB_2/air discharge product.— The ~30 mAh cells yield sufficient discharge product for effective FTIR and XRD characterization. For these analyses, a pure 8 M KOH electrolyte was employed, rather than the previous 8 M electrolyte containing 4 M KOH and 4 M NaOH.[21] This change of electrolyte leads to no discernable change in the discharge voltage or to the coulombic efficiency, but provides a simpler (single cation) basis for the discharge product analysis. Effective XRD of the product requires a slow 2Θ scan (6 hours from 2Θ = 5 to 80) due to the high carbon (30% Timcal) content. Additionally, the data is sequentially averaged every 10 data points, which does not result in any peak loss and improves the signal to noise ratio.

The XRD of the deeply discharged 30 mAh VB_2/air cell product does not exhibit remaining VB_2 and provides a strong match to the Inorganic Crystal Structure Database (ICSD) online spectra of KVO_3 shown as the blue curve in Figure 4. It is clear that as predicted in the initial discharge mechanism, pentavalent vanadium is present, V(V), and in this case takes the form of the salt KVO_3. Interestingly, the boron product is not evident, presumably existing as an amorphous

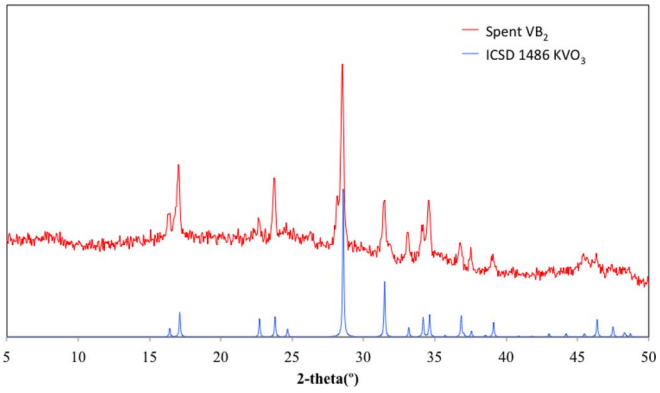

Figure 4. XRD comparison of the data point averaged VB_2/air 35 mAh discharge product as extracted from 3000 Ω discharged 1 cm diameter VB_2/air battery (top curve, red) and the library XRD spectra of KVO_3 (bottom curve, blue).

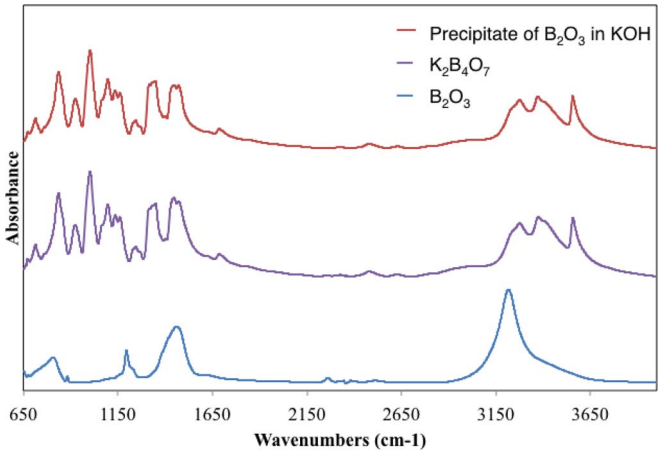

Figure 5. FTIR absorption (KBr pellet) spectra comparison of the precipitate formed from dissolving B_2O_3 in an 8M KOH solution to the initial solute, B_2O_3 while providing evidence of the predicted salt, $K_2B_4O_7$.

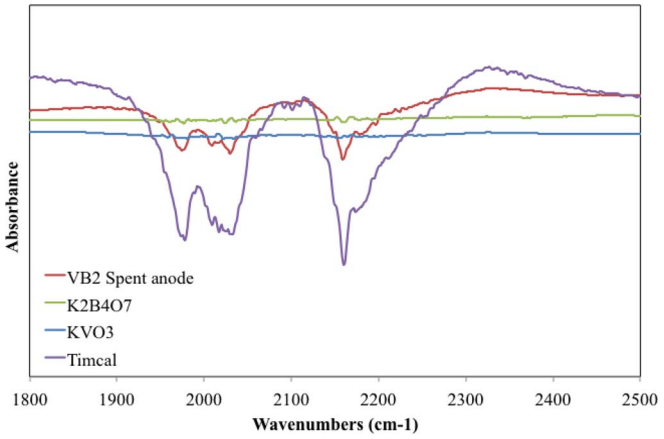

Figure 7. ATR FTIR comparison of Timcal C65 to the spent anodic material exhibiting features between 1900–2300 cm^{-1}.

rather than a crystalline product. In the subsequent section the boron product will be characterized by IR spectroscopy.

Solubility and IR of the VB_2/air discharge product.— The XRD analysis provides useful information of the vanadium product of the VB_2/air cell discharge. In order to determine the predominate boron species, further testing was performed via solubility analysis. Interestingly, one viable product, KVO_3, was found to be highly soluble (5.3 molar), whereas a boron product was found to exhibit a solubility behavior similar to zincate discharged in zinc/air batteries. In that latter case the solubility is dynamic, initially dissolving and then precipitating. Similarly, the equation 3 generalized predicted boron product, B_2O_3, was initially soluble in an 8M KOH, but after 48 hours had precipitated back out from solution. In order to determine the predominate boron species, further testing was performed prior to FTIR analysis. Vacuum filtration was used to collect the precipitate that was identified, via FTIR absorption analysis, to be potassium tetraborate tetrahydrate, $K_2B_4O_7$, shown in Figure 5. The formation of the precipitate from the battery electrolyte suggests that $K_2B_4O_7$, and not B_2O_3, is the principal B(+3) product when the VB_2/air cell is discharged in the KOH electrolyte.

Figure 6 compares FTIR absorption of the 30 mAh VB_2/air battery discharge product. As seen in Figure 6, the discharge product spectrum contains a mix of the separate pure component spectra of pure KOH, $K_2B_4O_7$ and KVO_3 (figure top), and the battery discharge product is a poor fit to the alternate alkali cation free and B_2O_3 and V_2O_3 products (figure bottom). The $K_2B_4O_7$ and KVO_3 products strongly overlap in the 650 to 1650 cm^{-1} domain. In the next section ATR FTIR is used to distinguish between these two product species.

ATR FTIR of the VB_2/air discharge product.— Although absent from the XRD pattern of the discharge product in Figure 4, ATR FTIR provides further evidence (in addition to the IR absorption evidence of Figures 5 and 6) of the boron product from the original VB_2 reactant. We hypothesize that the boron product is highly amorphous in character and it is therefore difficult to characterize with XRD. This hypothesis is supported by results comparing the ATR FTIR spectrum of the VB_2 discharged anode with that measured for KOH, B_2O_3, $K_2B_4O_7$, V_2O_5 and KVO_3. The ATR FTIR spectra in Figure 7 show the dominant feature between 1900 cm^{-1} and 2300 cm^{-1} is from the carbon added to the anode to improve electrical conductivity. The spectrum of this carbon, Timcal C65, is observed before the discharge and with or without mixing 70% by weight nanoscopic VB_2. Similarly as with the XRD analyses the high degree of absorption by this carbon black additive adds noise.

ATR FTIR over a broader frequency range was used for further comparison of the spent anodic material. The data shown in Figure 8 presents evidence for KVO_3 and $K_2B_4O_7$ as the primary discharge products extracted from an approximate 30 mAh discharged nanoscopic VB_2/air battery. Despite large variations to the baseline, due to Timcal there are notable absorption peaks, which provide evidence of the isolated discharge products. Spectral features located at approximately 825 cm^{-1}, 910 cm^{-1}, and 995 cm^{-1} show strong correlations between the spent battery material and $K_2B_4O_7$. Specifically, peaks at 680 cm^{-1} and 970 cm^{-1} may be attributed to KVO_3, rather

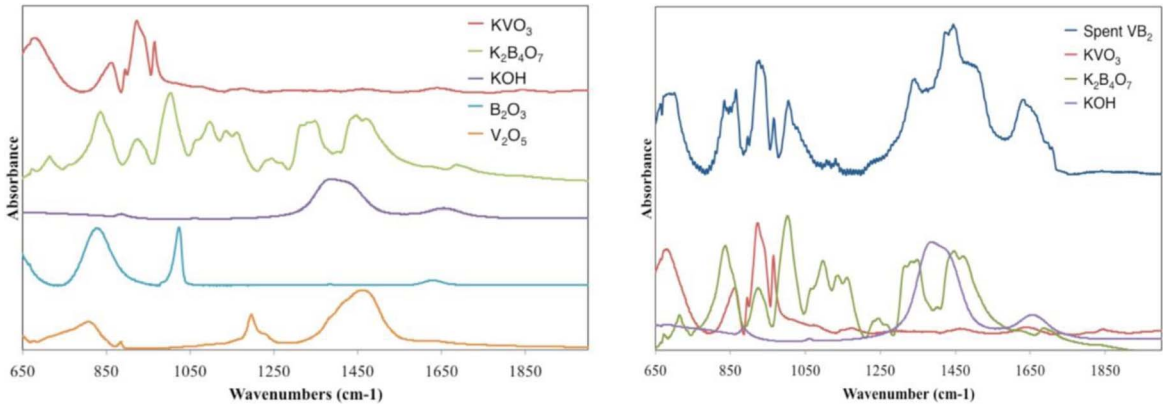

Figure 6. Left: FTIR absorption spectra comparison of the possible discharge products and 35 mAh VB_2/air battery discharge (spent) product. Right: FTIR absorption spectra of the product of the 35 mAh VB_2/air battery discharge compared to the individual FTIR of the has been suggested products $K_2B_4O_7$, KVO_3, and KOH.

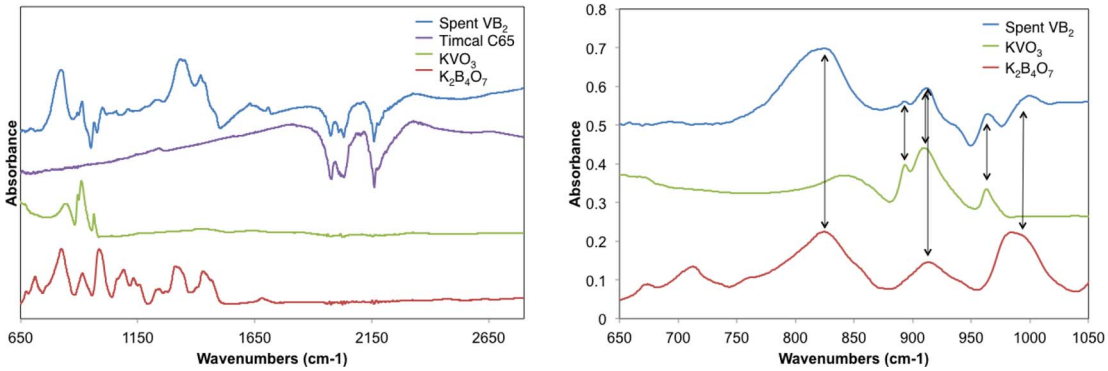

Figure 8. ATR FTIR analysis of the discharged VB_2/air battery anodic material to the expected discharge products, $K_2B_4O_7$ and KVO_3. (left) and (right) figures show region of 750–2800cm^{-1} and enlarged region 650–1050cm^{-1}, respectively.

than $K_2B_4O_7$. Additionally, features attributed to KVO_3 are located at 895 cm^{-1} and 910 cm^{-1}. This provides corroboration to the XRD evidence that KVO_3 is the principal vanadium discharge product of the VB_2/air battery, and is separate from the principal boron product, $K_2B_4O_7$.

There is little evidence for the IR absorption of B_2O_3 in the discharge product as shown in Figure 8, while the V_2O_5 spectrum in the figure exhibits general features evident in the discharge product. Absorption peaks in the 825 cm^{-1} and 995 cm^{-1} region overlap with features attributed to KVO_3 and $K_2B_4O_7$, respectively. Specific absorption peaks observed in the discharge product at 895 cm^{-1} and 910 cm^{-1} are not evident in the V_2O_5 spectrum. Despite uncertainties in the absorption baseline of the spent anodic material due to the large global IR absorption of the Timcal, these additional features are accounted for when KVO_3 is considered as the vanadium discharge product. From FTIR and ATR FTIR analysis of the spent anodic material and expected discharge products, it is evident that the VB_2/air discharge reaction is:

$$VB_2 + 11/4O_2 + 2KOH \rightarrow 1/2\ K_2B_4O_7 + KVO_3 + H_2O \qquad [4]$$

XPS probe of macroscopic VB_2 anode discharge.— Future work will show analysis of XPS measurements of charged and spent macroscopic VB_2. The discharged VB_2 samples are obtained from anodes equivalent to a capacity of 5 mAh of VB_2 and discharged at a load of 3000 ohm.

Conclusions

A mechanism for the net discharge process of the VB_2/air battery in the presence of a KOH electrolyte is presented. First experiments resulted in identification of KVO_3, a salt of the initial theorized V_2O_5 product. Solubility measurements provide significant evidence that the $K_2B_4O_7$ is the most probable borate product. From ATR FTIR analysis in KOH electrolyte, it is evident that the VB_2/air discharge products are $K_2B_4O_7$ and KVO_3. Our understanding of the discharge products of the electrooxidation of VB_2 provides a basis for further development of the unique multi-electron discharge processes of transition metal borides and related compounds.

In addition, the analysis of the unreacted (prior to discharge) VB_2 provides a better understanding of the higher observed discharge voltage of the nanoscopic compared to macroscopic anode VB_2/air batteries. X-ray photoelectron spectroscopy (XPS) measurements show that macroscopic and nanoscopic VB_2 materials have significantly different surfaces. The macroscopic VB_2 does not show the presence of VB_2 on the surface, but rather oxides. In contrast, the nanoscopic VB_2 shows the presence of VB_2 at the surface region. The surface oxides on the macroscopic VB_2 may result in an additional resistive layer, and this observation appears to be consistent with the lower voltage and capacity observed with those anodic materials. This work shows the significant impact of surface structure on electrochemical properties, and additional work will be aimed at understanding the factors that contribute to surface structure (e.g. synthetic conditions, particle size, surface coatings, atmospheric exposure time and temperature, etc.).

Coulombic efficiency of the VB_2 is high, but falls with increasing discharge current density. We have previously shown improvements and retention of high coloumbic efficiency using a zirconia coating of the VB_2.[12,17] We are currently investigating (i) solution phase additives, and (ii) an enhanced current collector conductive matrix to further advance the coulombic efficiency and maintain high stability for the VB_2/air battery. We are also exploring molten electrolytes to transition VB_2/air from a primary to a rechargeable battery.[25,26]

Acknowledgments

The authors are grateful for support of this study by the National Science Foundation (Award 1006568), the Air Force (SBIR award FA8650-13-C-5174), and the Welsh Foundation (AI-0045).

References

1. D. Linden and T. B. Reddy, *Handbook of Batteries*, 3rd edition. New York: McGraw-Hill (2002).
2. Z. Rogulski and A. Czerwiński, *J. Solid State Electrochem.* **7**, 118 (2003).
3. V. Neburchilov, H. Wang, J. J. Martin, and W. Qu, *J. Power Sources*, **195**, 1271 (2010).
4. X.-P. Gao and H.-X. Yang, *Energy Environ. Sci.* **3**,174 (2010).
5. S. Licht, G. Hodes, R. Tenne, and J. Manassen, *Nature*, **326**, 863 (1987).
6. D. Peramunage and S. Licht, *Science*, **261**, 1029 (1993).
7. S. Licht, B. Wang, and S. Ghosh, *Science*, **285**, 1039 (1999).
8. S. Licht, *Electrochem. Comm.*, **1**, 33 (1999).
9. R. Tel-Vered, G. Levitin, and S. Licht, *J. Electrochem. Soc.*, **147**, 496 (2000).
10. G. Levitin, C. Yarnitzky, and S. Licht, *Electrochem. Solid-State Lett.*, **5**, A160 (2002).
11. S. Licht, Y. Wang, and G. Gourdin, *J. Phy. Chem., C*, **113**, 9884 (2009).
12. S. Licht, X. Yu, and Y. Wang, *J. Electrochem. Soc.*, **155**, A1 (2008).
13. S. Licht, X. Yu, and D. Qu, *Chem. Comm.*, 2753 (2007).
14. S. Licht, X. Yu, Y. Wang, and H. Wu, *J. Electrochem. Soc.*, **155**, A297 (2008).
15. H. Yang, Y. Wang, X. Ai, and C. Cha, *Electrochem. Sol. State. Lett.*, **7**, A212 (2004).
16. Y. Wang, X. Ai, Y. Cao, and H. Yang, *Electrochem. Comm.*, **6**, 780 (2004).
17. S. Licht, H. Wu, X. Yu, and Y. Wang, *Chem. Comm.*, 3257 (2008).
18. S. Light, S. Ghosh, B. Wang, D. Jiang, J. Asercion, and H. Bergmann, *Electrochem. Solid State Lett.* **14**, A83 (2011).
19. S. Licht, C. Hettige, J. Lau, U. Cubeta, H. Wu, J. Stuart, and B. Wang, *Electrochem. Solid-State Lett.* **15**, A1 (2012).
20. C. Rhodes, J. Stuart, R. Lopez, X. Li, M. Waje, M. Mullings, J. Lau, and S. Licht, *J. Power Sources*, **239**, 244 (2013).
21. J. Stuart, R. Lopez, J. Lau, X. Li, M. Waje, M. Mullings, C. Rhodes, and S. Licht, *JOVE, J. Vis. Exp.*, 78, e50593 (2013).
22. V. Caramia and B. Bozzini, *Mater. Renew. Sustain. Energy*, **3**(28), 12 (2014).
23. L. Shi, Y. Gu, L. Chen, Z. Yang, J. Ma, and Y. Qian, *Mat. Lett.*, **58**, 2890 (2004).
24. C.D. Wagner, A.V. Naumkin, A. Kraut-Vass, J.W. Allison, C.J. Powell, and J.R. Rumble Jr., NIST Standard Reference Database 20, Version 4.1 (web version) (http:/srdata.nist.gov/xps/) 2012.
25. S. Licht, B. Cui, J. Stuart, B. Wang, and J. Lau, *Energy Environ. Sci.* **6**, 3646 (2013).
26. B. Cui and S. Licht, *J. Mat. Chem. A*, **2**, 10577 (2014).